Shear rate threshold for the boundary slip in dense polymer films

Nikolai V. Priezjev
Department of Mechanical Engineering, Michigan State University, East Lansing, Michigan 48824, USA
(Received 15 June 2009; published 24 September 2009)

The shear rate dependence of the slip length in thin polymer films confined between atomically flat surfaces is investigated by molecular dynamics simulations. The polymer melt is described by the bead-spring model of linear flexible chains. We found that at low shear rates the velocity profiles acquire a pronounced curvature near the wall and the absolute value of the negative slip length is approximately equal to the thickness of the viscous interfacial layer. At higher shear rates, the velocity profiles become linear and the slip length increases rapidly as a function of shear rate. The gradual transition from no-slip to steady-state slip flow is associated with faster relaxation of the polymer chains near the wall evaluated from decay of the time autocorrelation function of the first normal mode. We also show that at high melt densities the friction coefficient at the interface between the polymer melt and the solid wall follows a power-law decay as a function of the slip velocity. At large slip velocities the friction coefficient is determined by the product of the surface-induced peak in the structure factor, the temperature, and the contact density of the first fluid layer near the solid wall.

DOI: 10.1103/PhysRevE.80.031608 PACS number(s): 68.08.−p, 83.80.Sg, 83.50.Rp, 47.61.−k

I. INTRODUCTION

The rheology of complex fluids in thin films is important for theoretical and experimental studies of such common phenomena as friction, lubrication and wear [1]. Experimental measurements of the flow profiles and shear stresses on submicron scales might be subject to errors due to the possibility of liquid slip at the solid wall. An accurate prediction of flow, therefore, requires specification of a proper boundary condition. In the Navier model the interfacial shear rate and slip velocity are related via the proportionality coefficient, the so-called *slip length*. When the adjacent fluid layer slides past a solid wall with a finite velocity, the slip length is computed by linear extrapolation of the velocity profile near the interface to zero velocity [see Fig. 1(a)]. In the case when there is no relative velocity between fluid and solid at the interface, the formation of a lower viscosity boundary layer might result in the apparent slip length, which is defined by the slope of the bulk velocity profile [2] [see Fig. 1(b)]. Experimental studies on pressure-driven flows in microchannels or thin-film drainage using either the surface force apparatus or the atomic force microscope have demonstrated that the slip length depends on the nanoscale surface roughness [3–6], surface wettability [7–9], rate of shear [3,10–14], and fluid structure [15,16]. Several slip regimes exist due progressive disentanglement of the anchoring chains in the shear flow of polymer melts [17,18]. The difficulty in experimental determination of the velocity profiles and structure of complex fluids near interfaces leaves open important questions regarding the shear rate dependency of the slip length and the existence of a shear rate threshold for the boundary slip.

In the last two decades, the boundary conditions at the interface between monatomic liquids and atomically flat walls were extensively studied by molecular dynamics (MD) simulations [19–28]. The main factors affecting the slip are the energy of wall-fluid interaction and commensurability of the liquid and solid structures at the interface. At high wall-fluid energies, the first layer of fluid monomers becomes epitaxially locked to the solid substrate and the effective no-slip boundary plane is displaced into the fluid region. The absolute value of the negative slip length is approximately equal to the number of stacked monolayers between the effective and real boundary planes [19,21]. At low surface energy, the first layer can slide with a finite velocity relative to the solid substrate under the shear stress from the bulk fluid [this situation is sometimes referred to as a molecular or "true" slip, e.g., see Fig. 1(a)]. The slip length is inversely proportional to the peak of the in-plane structure factor computed in the first fluid layer at the main reciprocal lattice vector [21,23,27]. The exact relation between the slip length and microscopic parameters of the liquid/solid interface, however, has not yet been established.

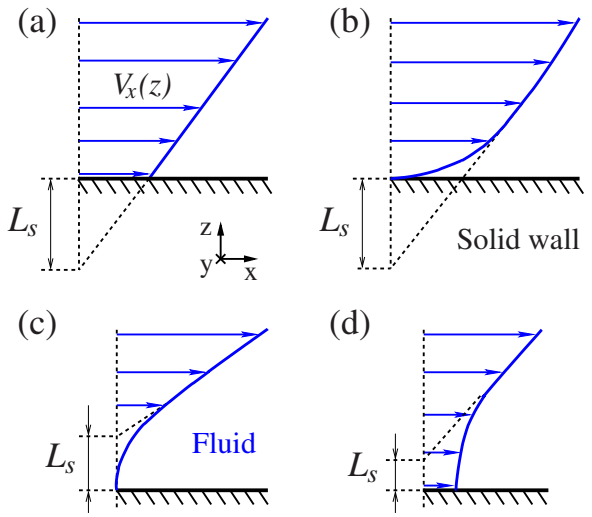

FIG. 1. (Color online) A schematic of a steady-state shear flow over a flat solid wall. (a) The slip velocity and the slope of the linear velocity profile are related via $V_s = \dot{\gamma} L_s$, where L_s is the slip length. (b) Apparent slip is associated with the lower viscosity boundary layer. (c) The velocity profile with a downward curvature due to higher viscosity boundary layer is described by the negative slip length. (d) A combination of the "true" slip at the liquid/solid interface and the curvature of the velocity profile.

The variation of the slip length with increasing shear rate in the flow of simple fluids past atomically smooth walls was first reported in the MD study by Thompson and Troian [29]. The nonlinear rate dependence of the slip length was well fitted by a power-law function for different wall densities and weak wall-fluid interaction energies [29]. In a later study [27], it was shown that the slip length is a linear function of shear rate at high wall-fluid interaction energies and, when the surface energy is reduced, the rate dependence of the slip length can be well fitted by the power-law function proposed in Ref. [29]. It was also found that in a wide range of shear rates and wall-fluid interaction energies, the slip length is a function of a single variable which combines the temperature of the first fluid layer, the contact density, and the peak value of the in-plane fluid structure factor evaluated at the main reciprocal lattice vector [27]. The results of previous MD studies of monatomic fluids lead to a conclusion that the boundary conditions for flows past smooth surfaces are either no-slip and rate independent [21], or described by the finite positive slip length that increases with shear rate [27–29]. Except for flows of low density fluids [30], there was no reported observation of a transition from no-slip to steady-state slip flow with increasing shear rate for simple fluids.

The slip length in a flow of a polymer melt past a flat passive (nonadsorbing) surface is a ratio of the fluid viscosity to the friction coefficient, which is determined by the interaction between fluid monomers and wall atoms [31]. In a recent MD study of unentangled melts confined between smooth surfaces [32], it was found that the friction coefficient at the liquid/solid interface is nearly independent of the chain length beyond ten bead-spring units and, therefore, the molecular weight dependence of the slip length at low shear rates is mostly dominated by the melt viscosity. Depending on the strength of the wall-fluid interaction energy, the slip occurs either at the confining surfaces [32–43] or between the adsorbed layer and free polymer chains [33,35]. A transition from stick to slip flow with increasing shear rate was reported in MD simulations of thin films of hexadecane [39] and oligomers [35] confined between strongly adsorbing surfaces. Despite extensive efforts in molecular simulations of thin polymer films, it still remains unclear what system parameters (fluid density, pressure, chain length, surface energy) determine the onset of boundary slip at the interface between an unentangled melt and a flat surface.

In a previous MD study [40], the effect of shear rate on slip boundary conditions in thin polymer films confined between atomically smooth surfaces was investigated as a function of melt density. It was found that the slip length, extracted from the linear velocity profiles, passes through a local minimum at low shear rates and then increases rapidly at higher shear rates. This behavior was rationalized in terms of the friction coefficient (defined as a ratio of the shear-thinning viscosity to the slip length), which undergoes a gradual transition from a nearly constant value to the power-law decay as a function of the slip velocity. The functional form of the relation between the friction coefficient and the slip velocity in the crossover region can also be considered as a boundary condition for monatomic fluids [29,40]. In addition, it was shown that in a wide range of shear rates and melt densities, the friction coefficient is determined by the product of the value of surface-induced peak in the structure factor, the temperature, and the contact density of the first fluid layer near the solid wall [40]. Whether these conclusions remain valid at higher melt densities (when a viscous interfacial layer is formed near the confined surfaces) is one of the motivations of the present study.

In this paper, we investigate the rate dependence of the slip length at the interface between an unentangled polymer melt and atomically flat walls using molecular dynamics simulations. We will show that in dense polymer films the velocity profiles are curved at low shear rates [shown schematically in Figs. 1(c) and 1(d)] due to the formation of a highly viscous interfacial layer and the corresponding slip length is negative. When the viscosity of the interfacial layer is reduced at higher shear rates, the velocity profiles become linear and the slip length increases rapidly as a function of shear rate. The relaxation dynamics of polymer chains near the walls and in the bulk region is studied by analyzing the time autocorrelation function of the first normal mode at equilibrium and in shear flow. We will also show that the friction coefficient follows a power-law decay as a function of the slip velocity and its universal dependence on microscopic parameters of the liquid/solid interface holds only at large slip velocities.

The rest of this paper is organized as follows. The details of molecular dynamics simulations and the equilibration procedure are described in the next section. The fluid velocity and density profiles, the shear rate dependence of the slip length, and the analysis of the fluid structure and relaxation dynamics of polymer chains are presented in Sec. III. The conclusions are given in the last section.

II. MOLECULAR-DYNAMICS SIMULATION MODEL

The simulation setup is similar to that described in the previous study [40] of a polymeric fluid undergoing planar shear flow between two atomically smooth walls. Figure 2 shows a snapshot of an unentangled polymer melt confined between solid walls. The total number of fluid monomers is kept the same as in the previous study (N_f=6000) but the simulations are performed at higher fluid densities. The fluid monomers interact via the truncated Lennard-Jones (LJ) potential

$$V_{LJ}(r) = 4\varepsilon\left[\left(\frac{\sigma}{r}\right)^{12} - \left(\frac{\sigma}{r}\right)^{6}\right] \quad \text{for} \quad r \le r_c = 2.5\sigma, \quad (1)$$

where ε and σ are the energy and the length scales of the fluid phase. The interaction between the wall atoms and fluid monomers is also modeled by the LJ potential with $\varepsilon_{wf}=0.9\varepsilon$ and $\sigma_{wf}=\sigma$. The wall atoms are tethered about the sites of an fcc lattice and do not interact with each other.

The coarse-grained bead-spring model was used to represent an unentangled polymer melt with linear chains of $N=20$ monomers. In addition to the LJ potential any two neighboring monomers in the chain interact through the finitely extensible nonlinear elastic (FENE) potential [44]

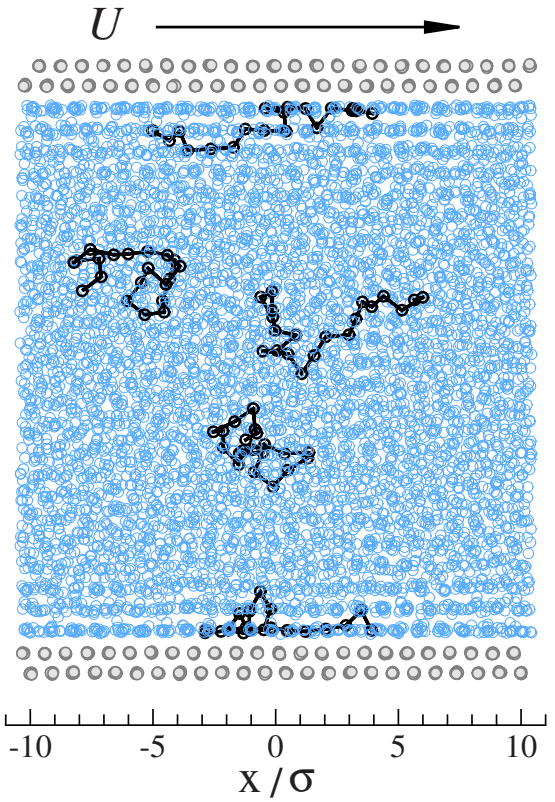

FIG. 2. (Color online) A snapshot of fluid monomers (open blue circles) and wall atoms (filled gray circles) positions projected on the xz plane. The bottom wall is at rest and the top wall is moving with a constant velocity U in the $\hat{x}$ direction. Each fluid monomer belongs to a polymer chain. Five polymer chains are marked by solid lines. The fluid monomer density is $\rho=1.08\sigma^{-3}$ and the top wall speed is $U=0.1\sigma/\tau$.

$$V_{\mathrm{FENE}}(r) = -\frac{k_s}{2} r_o^2 \ln[1 - r^2/r_o^2], \tag{2}$$

with the standard parameters $k_s=30\varepsilon\sigma^{-2}$ and $r_o=1.5\sigma$ [45]. A combination of LJ and FENE potentials between neighboring monomers yields an effective spring potential, which is strong enough to prevent polymer chains from unphysical crossing each other or bond breaking even at the highest shear rates considered in the present study.

The dynamics of fluid molecules and wall atoms was weakly coupled to a heat bath through a Langevin thermostat [46]. The thermostat was applied only to the $\hat{y}$ component (perpendicular to the plane of shear) of the equations of motion for fluid monomers to avoid a bias in the shear flow direction [21]. The equations of motion for fluid monomers in the $\hat{x}$, $\hat{y}$, and $\hat{z}$ directions are given by

$$m\ddot{x}_i = -\sum_{i\neq j} \frac{\partial V_{ij}}{\partial x_i}, \tag{3}$$

$$m\ddot{y}_i + m\Gamma\dot{y}_i = -\sum_{i\neq j} \frac{\partial V_{ij}}{\partial y_i} + f_i, \tag{4}$$

TABLE I. The fluid density ρ and pressure P at equilibrium ($U=0$). The density is defined as a ratio of the total number of fluid monomers ($N_f=6000$) to the volume $20.86\sigma\times 12.04\sigma\times(h-\sigma)$, where h is the distance between the fcc lattice planes in contact with the fluid.

ρ (units of σ^{-3})	1.04	1.06	1.08	1.09	1.11
P (units of $\varepsilon\sigma^{-3}$)	6.0	7.0	8.0	9.0	10.0
h (units of σ)	24.01	23.50	23.10	22.83	22.54

$$m\ddot{z}_i = -\sum_{i\neq j} \frac{\partial V_{ij}}{\partial z_i}, \tag{5}$$

where the sum is taken over the neighboring fluid monomers and wall atoms within the cutoff radius $r_c=2.5\sigma$, $\Gamma=1.0\tau^{-1}$ is the friction coefficient, and f_i is a random uncorrelated force with zero mean and variance $\langle f_i(0)f_j(t)\rangle=2mk_BT\Gamma\,\delta(t)\,\delta_{ij}$ determined from the fluctuation-dissipation relation. The temperature of the Langevin thermostat is set to $T=1.1\varepsilon/k_B$, where k_B is the Boltzmann constant. The equations of motion were integrated using the fifth-order gear-predictor algorithm [47] with a time step $\Delta t=0.002\tau$, where $\tau=\sqrt{m\sigma^2/\varepsilon}$ is the characteristic time of the LJ potential. The relatively small time step was chosen to resolve accurately the dynamics of fluid molecules and wall atoms at the interface.

The fluid is confined by the flat solid walls in the $\hat{z}$ direction (see Fig. 2). Each wall consists of 576 LJ atoms arranged in two layers of an fcc crystal with (111) plane parallel to the xy plane. The nearest-neighbor distance between fcc lattice sites in the xy plane is $d=1.0\sigma$ and the wall density is $\rho_w=1.40\sigma^{-3}$. The wall atoms were allowed to oscillate about their equilibrium lattice positions under the harmonic potential $V_{sp}=\frac{1}{2}\kappa r^2$ with the spring stiffness $\kappa=1200\varepsilon/\sigma^2$. The mean-square displacement of the wall atoms satisfies the Lindemann criterion for melting, i.e., $\langle\delta u^2\rangle/d^2\lesssim 0.023$. In addition, the random force and the damping term were applied to all three components of the wall atom equations of motion, e.g., for the $\hat{x}$ component

$$m_w\ddot{x}_i + m_w\Gamma\dot{x}_i = -\sum_{i\neq j} \frac{\partial V_{ij}}{\partial x_i} - \frac{\partial V_{sp}}{\partial x_i} + f_i, \tag{6}$$

where the mass of the wall atoms is $m_w=10m$, the friction coefficient is $\Gamma=1.0\tau^{-1}$, and the sum is taken over the fluid monomers within the cutoff distance $r_c=2.5\sigma$. Periodic boundary conditions were applied in the $\hat{x}$ and $\hat{y}$ directions parallel to the walls.

The polymer melt was initially equilibrated for about $5\times10^4\tau$ at a constant normal pressure $P=0.5\varepsilon\sigma^{-3}$ applied on the upper wall while the lower wall was kept at rest. Then, the external pressure was gradually increased to a desired value (reported in Table I). The distance between the walls was fixed after the system was additionally equilibrated at the constant pressure for about $2\times10^4\tau$. The MD simulations described below were performed at a constant density ensemble. The fluid density, the corresponding pressure in the absence of shear flow, and the channel height are listed in Table I.

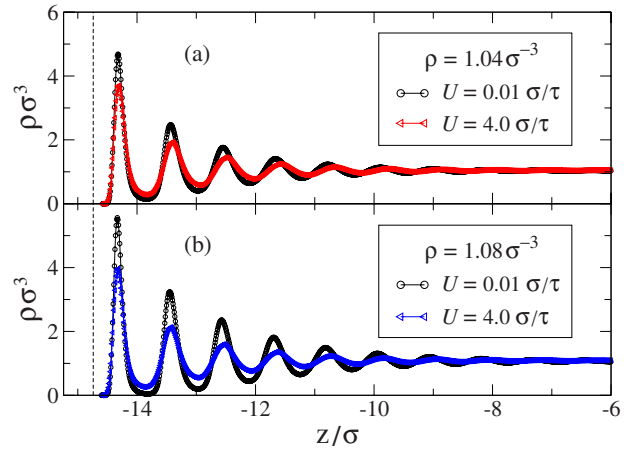

FIG. 3. (Color online) Averaged monomer density profiles near the stationary lower wall with $\varepsilon_{wf}/\varepsilon=0.9$. The uniform fluid densities away from the walls are (a) $\rho=1.04\sigma^{-3}$ and (b) $\rho=1.08\sigma^{-3}$. The upper wall velocities U are tabulated in the inset. The left vertical axis indicates the location of the fcc lattice plane at $z=-15.24\sigma$. The dashed line at $z=-14.74\sigma$ denotes the reference plane for computing the slip length.

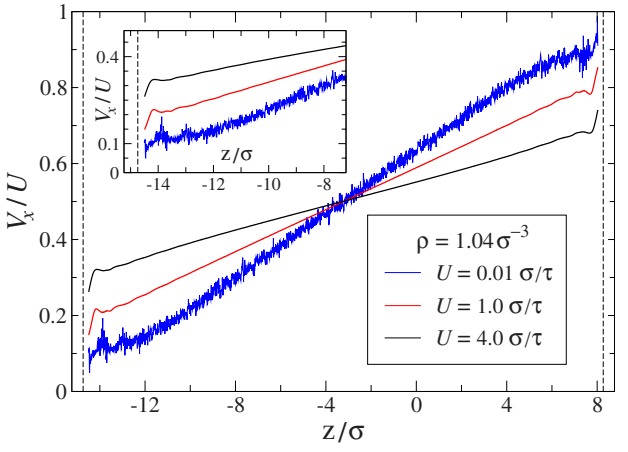

FIG. 4. (Color online) Average normalized velocity profiles for the indicated values of the upper wall speed and the fluid density $\rho=1.04\sigma^{-3}$. The vertical axes coincide with the position of the fcc lattice planes at $z=-15.24\sigma$ and $z=8.77\sigma$. The dashed lines denote liquid/solid interfaces at $z=-14.74\sigma$ and $z=8.27\sigma$. The inset shows an enlarged view of the velocity profiles near the stationary lower wall.

The shear flow was generated by moving the upper wall with a constant velocity U in the $\hat{x}$ direction parallel to the stationary lower wall. Before the production run started, the flow was simulated for about $5\times10^4\tau$ for each value of the upper wall speed. The fluid velocity and density profiles were averaged within bins of thickness $\Delta z=0.01\sigma$ for a time period up to $6\times10^5\tau$ at the lowest upper wall speed $U=0.001\sigma/\tau$. The small bin size was chosen to resolve accurately the velocity profiles and the fluid structure near the walls. At the highest shear rates examined in this study, the Reynolds number did not exceed the value $\mathrm{Re}\approx1.8$ estimated from the maximum difference of the fluid velocities near the upper and the lower walls, the shear viscosity, the fluid density, and the channel height (see Table I).

III. RESULTS

A. Fluid density and velocity profiles

Molecular simulations of polymer melts confined by flat walls have demonstrated that the fluid structure consists of several discrete layers of monomers, the polymer chains are flattened near the walls, and the chain configurations remain bulklike in a region of several molecular diameters away from the walls [48]. Qualitatively, these features can be observed in the snapshot of the polymer film shown in Fig. 2. Note that the first two layers of monomers near the walls are clearly distinguishable, the polymer chains in contact with the wall atoms are compressed toward the interface and their constitutive monomers are located within the discrete layers.

The representative density profiles are shown in Fig. 3 for $\rho=1.04\sigma^{-3}$ and $\rho=1.08\sigma^{-3}$ and two values of the upper wall speed. The density oscillations extend to a distance of about $5\sigma-6\sigma$ from the walls and the profiles are uniform in the central bulk region. The magnitude of the first peak near the wall defines a contact density ρ_c. The amplitude of the density oscillations is reduced with increasing upper wall speed. Notice that at low U in the case $\rho=1.08\sigma^{-3}$ shown in Fig. 3(b), the local density minimum between the first and the second peaks is almost zero. It implies that the fluid monomers rarely jump between the first two layers, and it is, therefore, expected that the averaged velocity profiles will have relatively poor statistics in that region (see below).

Figure 4 shows the averaged velocity profiles in steady-state flow for the lowest fluid density ($\rho=1.04\sigma^{-3}$) considered in this study. The velocity profiles remain linear throughout the channel except for a larger slope inside the first fluid layer. A finite slip velocity is noticeable even at very low upper wall speed $U=0.01\sigma/\tau$. The data are noisy because the averaged velocity component in the $\hat{x}$ direction is much smaller than the thermal fluid velocity $v_T^2=k_BT/m$. The velocity profile for $U=0.01\sigma/\tau$ bends slightly near the walls, which implies that the interfacial viscosity is higher than the fluid viscosity in the bulk region. A small curvature in the bulk region of the velocity profile at $U=4\sigma/\tau$ might be related to the nonuniform heating up of the fluid at high shear rates [40]. The normalized slip velocity increases with increasing upper wall speed.

The averaged velocity profiles at the higher melt density ($\rho=1.08\sigma^{-3}$) are reported in Fig. 5. At small values of the upper wall speed, the slip velocity of the first fluid layer is barely noticeable and the profiles are highly curved near the walls due to the presence of the viscous interfacial layer with thickness of about $2\sigma-3\sigma$. The statistical fluctuations are relatively large near the walls because of the pronounced density layering [e.g., see Fig. 3(b)]. The effective no-slip boundary plane is located inside the fluid domain at a distance of about 2σ from the wall. With increasing upper wall speed, the fluid velocity profiles become linear, the no-slip boundary plane is displaced out of the fluid region, and the slip velocity increases.

The normalized velocity profiles for the highest fluid density $\rho=1.11\sigma^{-3}$ are plotted in Fig. 6. At the lowest upper wall

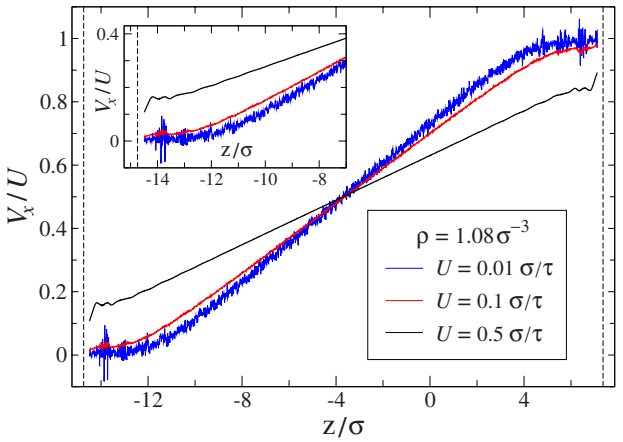

FIG. 5. (Color online) Averaged velocity profiles for the indicated upper wall speeds U (in units of σ/τ) and the fluid density $\rho=1.08\sigma^{-3}$. The vertical axes indicate the location of the fcc lattice planes at $z=-15.24\sigma$ and $z=7.86\sigma$. The dashed lines denote the position of the liquid/solid interfaces 0.5σ away from the fcc planes. The region near the lower wall is enlarged in the inset.

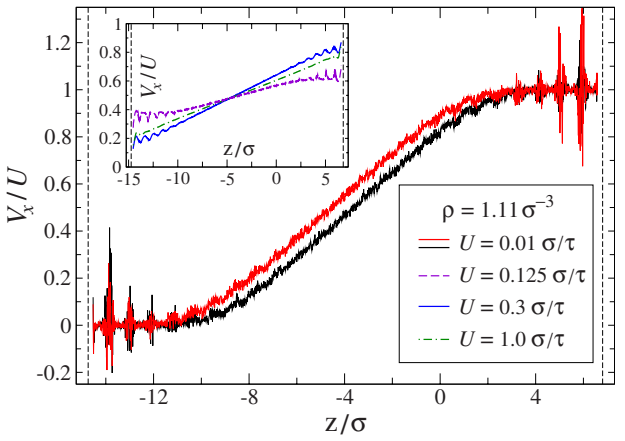

FIG. 6. (Color online) Average normalized velocity profiles for the upper wall speed $U=0.01\sigma/\tau$ (see text for description). The vertical dashed lines indicate liquid/solid interfaces at $z=-14.74\sigma$ and $z=6.81\sigma$. The inset shows averaged velocity profiles for the upper wall speeds $U=0.125\sigma/\tau$ (dashed violet curve), $U=0.3\sigma/\tau$ (continuous blue curve), and $U=1.0\sigma/\tau$ (dashed-dotted green line).

speed $U=0.01\sigma/\tau$, the first four monolayers stick to the walls but the velocity profiles remain linear in the middle of the channel. Due to the low probability of finding chain segments in between the monolayers, the statistical uncertainties are much larger near the walls than in the bulk region. We found that the shape of the flow profiles depends on how the system was prepared. In one case, the upper wall speed was increased from zero to $U=0.01\sigma/\tau$ following the equilibration procedure described in the previous section. The averaged velocity profile is marked by the lower black curve in Fig. 6. In the other case, the upper wall speed was first increased to $U=0.5\sigma/\tau$ and then, after the equilibration period of about $10^5\tau$, gradually reduced to $U=0.01\sigma/\tau$. The corresponding velocity profile is shown by the upper red curve in Fig. 6. Note that the width of the flowing regions is nearly the same in both cases but the thickness of the immobile interfacial layers varies from about four to five molecular diameters. We also found that at higher upper wall speeds ($0.1\lesssim U\tau/\sigma\lesssim 0.25$) the first fluid layer slides with a finite velocity past the substrate and the weak oscillations in the velocity profiles near the walls correlate well with the fluid density layering (see inset in Fig. 6). Finally, as shown in the inset of Fig. 6, the velocity profiles become linear throughout the channel at higher upper wall speeds ($U\gtrsim 0.3\sigma/\tau$) and the slip velocity increases monotonically with increasing U.

The slope of the linear part of the velocity profiles in the bulk region of the channel (6σ away from the walls) was used to compute the shear rate and the slip length. We define the slip length as a location of the point where linearly extrapolated velocity profile vanishes. Negative value of the slip length implies that the effective no-slip boundary plane is displaced into the bulk fluid domain. The velocity of the first fluid layer with respect to the lower stationary wall was computed as follows:

$$V_1 = \int_{z_0}^{z_1} V_x(z)\rho(z)dz \Big/ \int_{z_0}^{z_1} \rho(z)dz, \tag{7}$$

where the limits of integration ($z_0=-14.50\sigma$ and $z_1=-13.85\sigma$) were determined from the width of the first peak in the density profile. Note that even if the flow profiles are linear throughout the channel, the velocity of the first layer V_1 is slightly larger than the slip velocity computed from the Navier relation $V_s=\dot{\gamma}L_s$ (by about $0.5\dot{\gamma}$ in units of σ/τ). This is because the slip length is defined with respect to the reference plane 0.5σ away from the inner fcc lattice plane and the first fluid layer is located approximately σ away from the fcc plane (see Fig. 3).

B. Shear-rate dependence of the melt viscosity and slip length

We first estimate the polymer melt viscosity which is defined as a ratio of shear stress to shear rate, i.e., $\sigma_{xz}=\mu\dot{\gamma}$. The shear stress was computed using the Kirkwood relation [49] in the bulk region (6σ away from the confining walls), where the fluid structure is uniform and the velocity profiles are linear even at low shear rates. The viscosity is plotted in Fig. 7 as a function of shear rate for the indicated values of the polymer density. The Newtonian regime is observed only in a narrow range of shear rates, and it is followed by the crossover to the shear-thinning behavior, which occurs at higher shear rates when the melt density is reduced. The dashed line in Fig. 7 corresponds to the power-law decay with the exponent −0.37 reported for the lower density polymer melts ($0.86\lesssim\rho\sigma^3\lesssim 1.02$) at high shear rates [40]. The data presented in Fig. 7 indicate that the melt viscosity in the shear-thinning regime decreases faster at higher fluid densities. The statistical errors due to thermal fluctuations are relatively large at low shear rates.

The variation of the slip length as a function of shear rate is presented in Fig. 8 for all melt densities considered. As expected from the shape of the velocity profiles described in

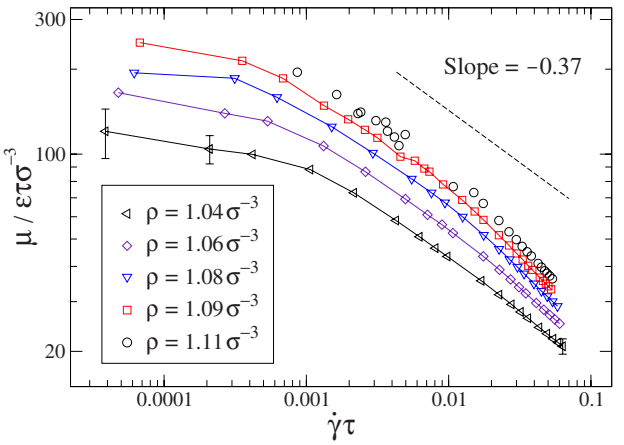

FIG. 7. (Color online) Shear-rate dependence of the viscosity in the bulk region $\mu/\varepsilon\tau\sigma^{-3}$ for the indicated values of the polymer density. The dashed line with a slope −0.37 is shown for reference. Solid curves are a guide for the eye.

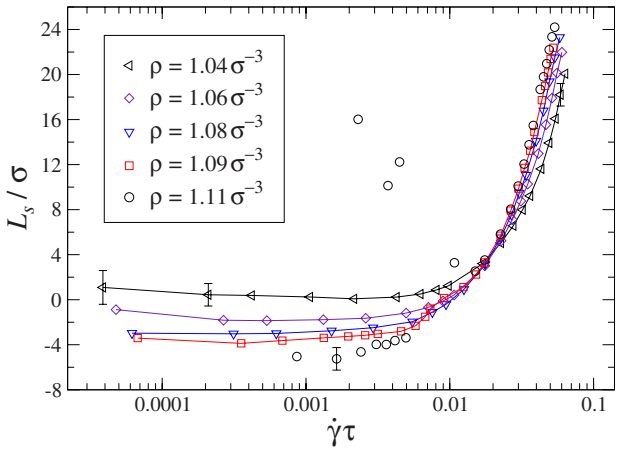

FIG. 8. (Color online) Slip length L_s/σ as a function of shear rate for the indicated values of the polymer melt density. At low shear rates and $\rho=1.11\sigma^{-3}$, the slip length is multivalued. Solid curves are drawn to guide the eye.

the previous section, the slip length at low shear rates is negative (except for $\rho=1.04\sigma^{-3}$) and its magnitude is approximately equal to the thickness of the viscous interfacial layer. With increasing shear rate, the velocity profiles become linear, implying that the local viscosity of the boundary layer is reduced, and the slip length increases rapidly. At the highest melt density $\rho=1.11\sigma^{-3}$ and low shear rates, the thickness of the interfacial layer depends on the equilibration procedure and the slip length cannot be uniquely defined. The uncertainty in the slip length related to the thickness of the immobile interfacial layer and the slope of the velocity profile in the bulk region is about 2σ. At higher upper wall speeds $(0.1\lesssim U\tau/\sigma\lesssim 0.25)$ and $\rho=1.11\sigma^{-3}$, the first fluid layer is sliding with a finite velocity and the slip length is relatively large. Multivalued slip lengths were also reported in shear flow of simple fluids past smooth surfaces with high wall-fluid interaction energy [21]. Finally, we comment that the data presented in Fig. 8 cannot be well fitted by the power-law function suggested in Ref. [29].

In our simulations, the upper wall speed was varied so that the slip velocity remains less than about the fluid thermal velocity. We performed test runs at higher upper wall speeds $(U\gtrsim 4\sigma/\tau)$ and observed a different regime, where the slip length becomes a nonmonotonic function of shear rate. It was also recently shown that the slip length at the interface between short chain polymers and smooth thermal walls approaches a constant value at high shear rates [50,51]. In the present study, the behavior of the slip length at very large slip velocities and high shear rates was not examined in detail.

The rate-dependent boundary conditions can be reformulated in terms of the wall shear stress and slip velocity. In the steady-state shear flow, the stress across any plane parallel to the confining walls is the same; and, therefore, the shear stress computed in the bulk region is equal to the wall shear stress. The slip velocity of the first fluid layer was calculated by averaging the velocity profile over the width of the first density peak using Eq. (7). Note that the slip velocity computed from the Navier relation $(V_s=\dot{\gamma}L_s)$ is smaller than V_1 or can be even negative if the velocity profiles are curved near the interface [e.g., see Figs. 1(c) and 1(d)]. The shear stress averaged in the bulk region is plotted in Fig. 9 as a function of the slip velocity of the first fluid layer for the indicated polymer melt densities. The shear stress increases rapidly at small slip velocities and grows steadily at large V_1. At the highest melt density $\rho=1.11\sigma^{-3}$, the time-averaged shear stress is discontinuous at small slip velocities.

The nonlinear relation between the shear stress and the slip velocity shown in Fig. 9 can be used to determine the friction coefficient per unit area $\sigma_{xz}=kV_1$ as a function of V_1. We comment that the ratio of the shear viscosity to the slip length cannot be used to compute the friction coefficient at the liquid/solid interface when the velocity profiles are curved near the surface and the slip length is extracted from the bulk part of the profiles. In the previous study [40], the simulations were performed at lower polymer melt densities and the velocity profiles remained linear at all shear rates examined. In the range of densities $(0.86\leq\rho\sigma^3\leq 1.02)$, the friction coefficient $(k=\mu/L_s)$ as a function of the slip velocity was well described by the following equation:

$$k/k^* = [1+(V_s/V_s^*)^2]^{-0.35}, \tag{8}$$

where k^* and V_s^* are the normalization parameters [40]. In the present study, the friction coefficient is plotted as a function of the slip velocity in Fig. 10. The data can be well fitted by the empirical formula (8) at lower melt densities $\rho\leq 1.06\sigma^{-3}$ (not shown). At higher melt densities $\rho\gtrsim 1.08\sigma^{-3}$, the plateau regime, where the friction coefficient is independent of the slip velocity, is absent and the slope of the power-law decay is slightly smaller than −0.7 (see the dashed line in Fig. 10).

C. Friction coefficient and fluid structure in the first layer

The connection between friction at the liquid/solid interface and fluid structure induced by the periodic surface potential was established for monatomic fluids [21,23,27,28,52,53], polymer melts [32,40], adsorbed mono-

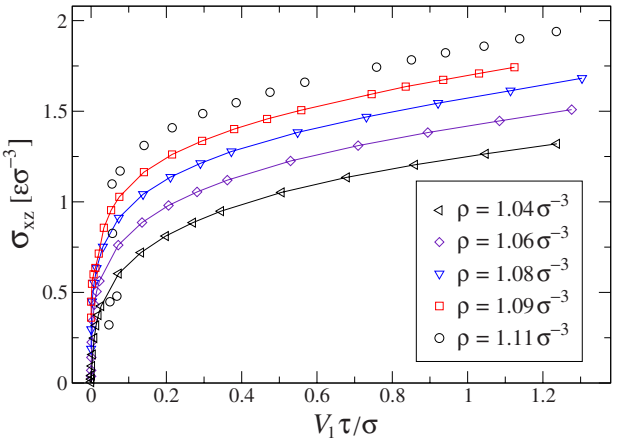

FIG. 9. (Color online) Shear stress σ_{xz} (in units of $\varepsilon\sigma^{-3}$) averaged in the bulk region as a function of the slip velocity of the first fluid layer for the indicated values of the polymer melt density. Solid curves are a guide for the eye.

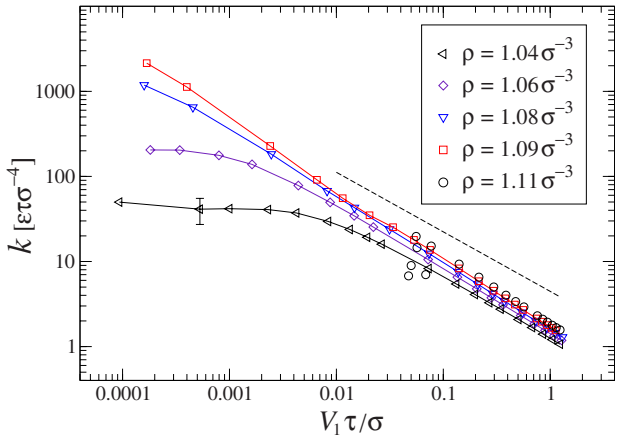

FIG. 10. (Color online) Log-log plot of the friction coefficient $k=\sigma_{xz}/V_1$ (in units of $\varepsilon\tau\sigma^{-4}$) as a function of the slip velocity [computed from Eq. (7)] for the tabulated values of the polymer density. The dashed line with a slope of −0.7 is plotted for reference. The same data as in Fig. 9. Solid curves are drawn as a guide for the eye.

layers [54,55], and adsorbed polymer layers [56]. The in-plane structure factor in the first fluid layer near the solid substrate is defined as

$$S(\mathbf{k}) = \frac{1}{N_\ell}\left|\sum_{j=1}^{N_\ell} e^{i\mathbf{k}\cdot\mathbf{r}_j}\right|^2, \tag{9}$$

where $\mathbf{r}_j=(x_j,y_j)$ is the position vector of the jth monomer and N_ℓ is the number of monomers within the layer [21]. Typically, the structure factor exhibits a circular ridge at the wave vector $|\mathbf{k}|\approx 2\pi/\sigma$ due to short-range ordering of the fluid monomers. In addition, at sufficiently high wall-fluid interaction energy, several sharp peaks appear in the structure factor at the reciprocal lattice vectors of the crystal wall. It is well established that the magnitude of the peak at the first reciprocal lattice vector in the shear flow direction correlates well with the friction coefficient at the interface between a simple LJ liquid and a solid wall composed out of periodically arranged LJ atoms [21,23,27].

In the present study, the first reciprocal lattice vector in the shear flow direction $\mathbf{G}_1=(7.23\sigma^{-1},0)$ is slightly displaced from the wave vector $|\mathbf{k}|\approx 2\pi/\sigma$. The averaged structure factor $S(\mathbf{G}_1)$ is plotted in Fig. 11(a) as a function of the slip velocity of the first fluid layer for the polymer density $\rho=1.08\sigma^{-3}$. The error bars are relatively large at small slip velocities due to the slow relaxation dynamics of the polymer chains in the interfacial layer (see the next section). At higher slip velocities, fluid monomers spend less time in the minima of the periodic surface potential; and, as shown in Fig. 11(a), the magnitude of the surface-induced peak in the structure factor decreases logarithmically with increasing V_1. Furthermore, as expected from the density profiles shown in Fig. 3 for different upper wall speeds, the contact density is reduced at higher slip velocities [see Fig. 11(b)]. Similarly to the definition of the slip velocity given by Eq. (7), the temperature of the first fluid layer was computed as follows:

$$T_1 = \int_{z_0}^{z_1} T(z)\rho(z)dz \Big/ \int_{z_0}^{z_1} \rho(z)dz, \tag{10}$$

where $T(z)$ is the local kinetic temperature and the limits of integration ($z_0=-14.50\sigma$ and $z_1=-13.85\sigma$) were determined from the width of the first density peak. The variation of the monolayer temperature as a function of the slip velocity is presented in Fig. 11(c). At small slip velocities $V_1 \lesssim 0.03\sigma/\tau$, the temperature is equal to value $T=1.1\varepsilon/k_B$ set by the Langevin thermostat. With increasing upper wall speed, the temperature of the first fluid layer gradually rises up to $T\approx 1.6\varepsilon/k_B$ at the highest slip velocity $V_1\approx 1.3\sigma/\tau$ reported in Fig. 11(c). At shear rates $\dot{\gamma}\gtrsim 0.01\tau^{-1}$, the tem-

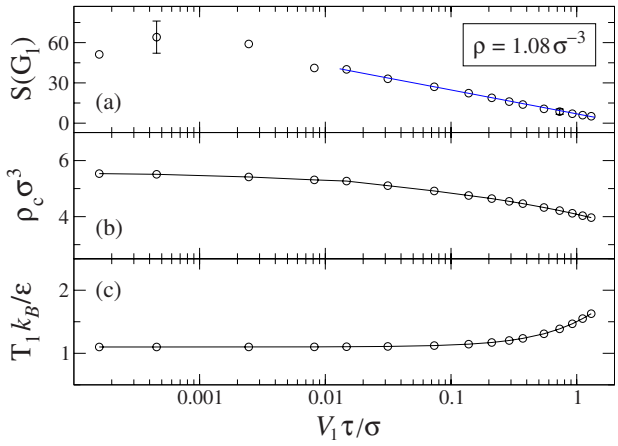

FIG. 11. (Color online) Structure factor $S(\mathbf{G}_1)$ evaluated at the first reciprocal lattice vector $\mathbf{G}_1=(7.23\sigma^{-1},0)$ in the shear flow direction (a), contact density near the stationary lower wall (b), and temperature (c) of the first fluid layer as a function of the slip velocity V_1 (in units of σ/τ). The solid blue line $y=6.93-7.73\ln(x)$ represents the best fit to the data. Solid curves are a guide for the eye.

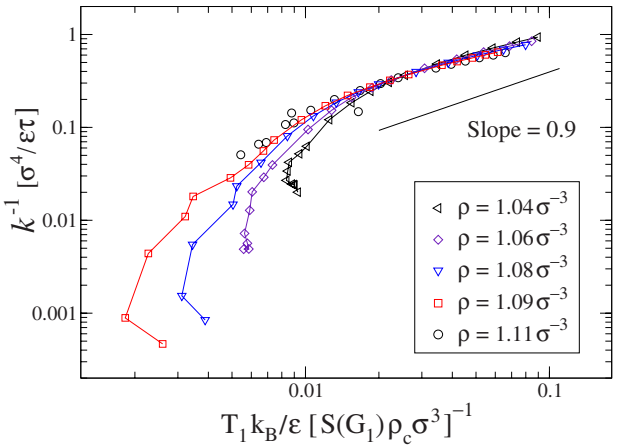

FIG. 12. (Color online) Log-log plot of the inverse friction coefficient $k^{-1}=V_1/\sigma_{xz}$ (in units of $\sigma^4/\varepsilon\tau$) as a function of $T_1k_B/\varepsilon[S(\mathbf{G}_1)\rho_c\sigma^3]^{-1}$ evaluated in the first fluid layer for the indicated polymer melt densities. The solid line with a slope of 0.9 is plotted as a reference.

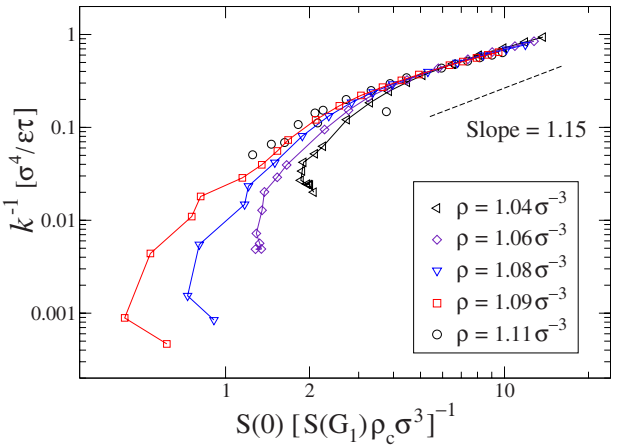

FIG. 13. (Color online) Log-log plot of the inverse friction coefficient $k^{-1}=V_1/\sigma_{xz}$ (in units of $\sigma^4/\varepsilon\tau$) as a function of the variable $S(0)/[S(\mathbf{G}_1)\rho_c\sigma^3]$ computed in the first fluid layer. The fluid densities are listed in the inset. The dashed line with a slope of 1.15 is shown for reference.

perature profiles across the channel $T(z)$ become nonuniform and the heating up is larger near the interfaces (e.g., see Fig. 9 in Ref. [40]).

The dependence of the friction coefficient on the structure factor, contact density, and temperature of the first fluid layer was studied in the recent paper [40] at lower polymer melt densities ($0.86\leq\rho\sigma^3\leq1.02$). Except for the densities $\rho=1.00\sigma^{-3}$ and $1.02\sigma^{-3}$ at low shear rates, the data for the friction coefficient ($k=\mu/L_s$) were found to collapse on master curves when plotted as a function of either $T_1/[S(\mathbf{G}_1)\rho_c]$ or $S(0)/[S(\mathbf{G}_1)\rho_c]$. In both cases, the data could be well fitted by a power-law function with the exponents −0.9 and −1.15, respectively [40]. At higher polymer densities ($1.04\leq\rho\sigma^3\leq1.11$) considered in the present study, the inverse friction coefficient is plotted in Figs. 12 and 13 as a function of the combined variables $T_1/[S(\mathbf{G}_1)\rho_c]$ and $S(0)/[S(\mathbf{G}_1)\rho_c]$, respectively. The collapse of the data holds at small values of the friction coefficient $k\lesssim4\varepsilon\tau\sigma^{-4}$ and the surface-induced peak in the structure factor $S(\mathbf{G}_1)\lesssim14$. Thus, the simulations at higher melt densities provide an upper bound for the friction coefficient ($k\approx4\varepsilon\tau\sigma^{-4}$), below which the data are described by a single master curve [40]. These results support the conclusion from the previous studies that at the interface between an atomically smooth solid wall and a simple [27] or polymeric [40] fluid, the friction coefficient is determined by a combination of parameters evaluated in the first fluid layer.

D. Relaxation dynamics of polymer chains

Equilibrium molecular dynamics studies of polymer melts confined between attractive walls have shown that the relaxation of polymer chains slows down near the interfaces and becomes bulklike at distances of about two radii of gyration away from the walls [57,58]. In order to probe the relaxation dynamics of polymer chains in shear flow, we evaluated the autocorrelation function of the normal modes in the direction perpendicular to the plane of shear. The $\hat{y}$ component of the normal coordinates for a discrete polymer chain of N monomers is given by

$$Y_p(t)=\frac{1}{N}\sum_{i=1}^{N}y_i(t)\cos\frac{p\pi(i-1)}{N-1}, \tag{11}$$

where y_i is the component of the position vector of the ith monomer in the chain and $p=0,1,\ldots,N-1$ is the mode number [59]. The longest relaxation time of a polymer chain is associated with the first mode $p=1$. The normalized time autocorrelation function for the first normal mode is computed as follows:

$$C_1(t)=\langle Y_1(t)Y_1(0)\rangle/\langle Y_1(0)Y_1(0)\rangle. \tag{12}$$

The relaxation dynamics in heterogeneous systems is usually described by the stretched exponential (or Kohlrausch-Williams-Watts) function $C_1(t)=\exp[-(t/\tau_1)^{\beta}]$. The time integral of the stretched exponential defines the characteristic decay time $\tau_y^*=\tau_1\Gamma(\beta^{-1})/\beta$, where Γ is the gamma function and β is the stretched exponential coefficient.

The autocorrelation function [Eq. (12)] was computed separately in the bulk region (6σ away from the solid walls) and inside the interfacial layers (within 3σ from the walls). During the simulation, the normal coordinate and the position of the center of mass of each polymer chain were calculated every 100τ, and the autocorrelation function was updated only if the position of the center of mass was inside either bulk or interfacial regions. The correlation function was averaged for at least $6\times10^5\tau$ at low shear rates to resolve very slow dynamics of the polymer chains near the interfaces.

Figure 14 shows the time autocorrelation function computed at equilibrium conditions (i.e., $U=0$) for the indicated polymer densities. As expected, the relaxation of the polymer chains in the bulk and near the walls is slower at higher melt densities. The inverse bulk relaxation time, estimated roughly from $C_1(t)=1/e$ in Fig. 14(a), correlates well with the onset of shear thinning of the fluid viscosity reported in

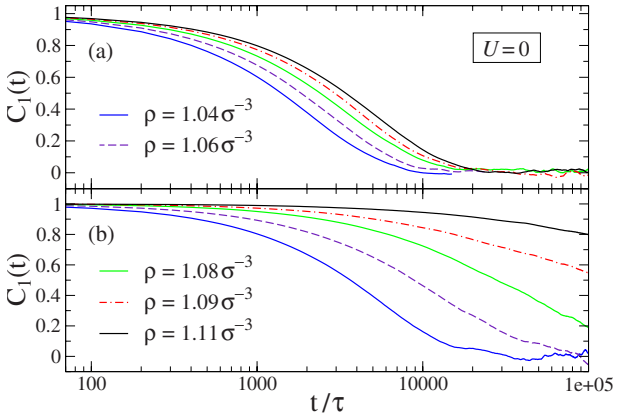

FIG. 14. (Color online) Normalized time autocorrelation function of the first normal mode at equilibrium for polymer chains (a) in the bulk region and (b) near the walls for the indicated values of the fluid density.

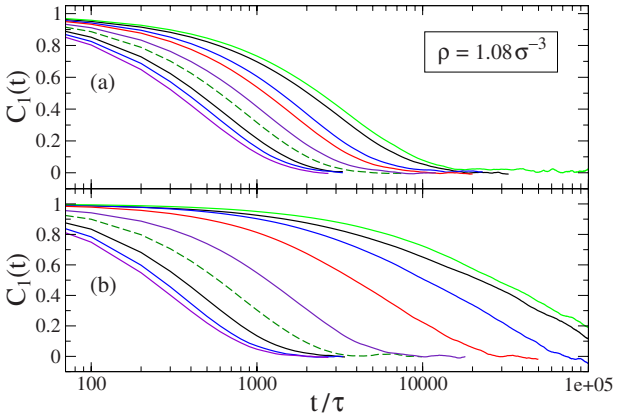

FIG. 15. (Color online) Time autocorrelation function of the first normal mode for polymer chains (a) in the bulk region and (b) near the walls and the fluid density $\rho=1.08\sigma^{-3}$. The upper wall speed from right to left is $U=0$, 0.025, 0.1, 0.2, 0.5, 1.0, 2.0, 3.0, and 4.0 (in units of σ/τ).

Fig. 7. For each density, the decay of the correlation function is slower for the chains in the interfacial layer than in the bulk of the channel. The difference in relaxation times is especially evident at higher melt densities, $\rho \geq 1.09\sigma^{-3}$, where only the early stage of relaxation is reported in Fig. 14(b). At the lowest polymer density $\rho=1.04\sigma^{-3}$, the decay time of the interfacial chains is about two to three times larger than in the bulk, which agrees with the conclusion drawn from the shape of the velocity profile for $U=0.01\sigma/\tau$ in Fig. 4 that the interfacial viscosity is higher than the bulk value.

The influence of shear flow on the time autocorrelation function is demonstrated in Fig. 15 for the polymer density $\rho=1.08\sigma^{-3}$. At low upper wall speeds $U \lesssim 0.1\sigma/\tau$, the relaxation dynamics near the interface is much slower than in the bulk region, implying the formation of a highly viscous interfacial layer. The spatial variation of the shear viscosity correlates with the nonlinearity in the velocity profiles shown in Fig. 5. When $U=1.0\sigma/\tau$, the decay time of the correlation function is nearly the same across the channel (see the dashed curves in Fig. 15) and the velocity profile is linear (shown for $U=0.5\sigma/\tau$ in Fig. 5). At higher upper wall speeds, the polymer chains relax slightly faster near the walls than in the bulk, possibly because of the heating up of the fluid near the walls.

Finally, the relaxation time of the polymer chains near the walls and the slip length are summarized in Fig. 16 as a function of shear stress and polymer density. The leftmost points of the curves shown in Fig. 16 correspond to the upper wall speed $U=0.01\sigma/\tau$. At low shear stress, the relaxation time varies widely (from $\tau_y^* \approx 6.2\times 10^2\tau$ at $\rho=1.04\sigma^{-3}$ to $\tau_y^* \approx 3.3\times 10^6\tau$ at $\rho=1.11\sigma^{-3}$), indicating the presence of a highly viscous boundary layer at higher melt densities. With increasing shear stress, the decay time decreases and, when $U \gtrsim 1.5\sigma/\tau$, the relaxation of the polymer chains near the walls becomes even slightly faster than in the bulk region (see also Fig. 15). The dependence of the inverse relaxation time on the shear stress exhibits qualitatively similar behavior to the slip length, which supports the conclusion (drawn from the shape of the velocity profiles) that the transition to slip flow is associated with the reduction of the fluid viscosity in the interfacial layer. The inset in Fig. 16 shows the variation of the stretched exponential coefficient as a function of shear stress. The data are scattered at low shear stress due to the slow relaxation of the polymer chains, and the decay of the autocorrelation function becomes nearly exponential at higher shear stress.

IV. CONCLUSIONS

In this paper, the rate dependence of the slip length at the interface between a dense polymer melt and weakly attractive smooth walls was studied using molecular dynamics simulations. The melt was modeled as a collection of linear chain polymers ($N=20$). It was shown that at low shear rates the velocity profiles are curved near the wall due to the formation of a highly viscous interfacial layer and the effective slip length is negative and almost rate independent. With

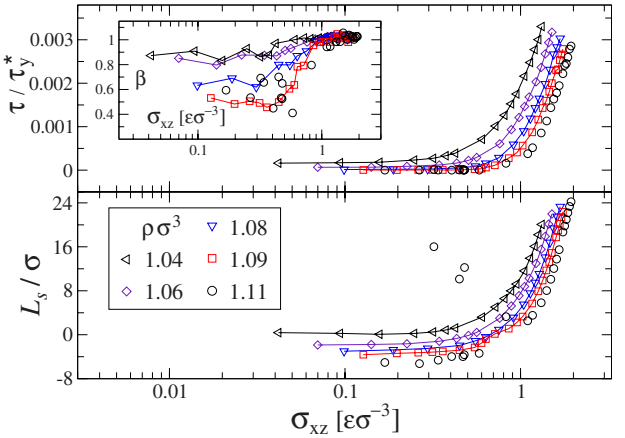

FIG. 16. (Color online) Inverse relaxation time of the polymer chains near the walls (top) and the slip length (bottom) as a function of shear stress σ_{xz} (in units of $\varepsilon\sigma^{-3}$) for the indicated values of the melt density. The inset shows the stretched exponential coefficient for the same data.

increasing upper wall speed, the gradual transition to steady-state slip flow is associated with the reduction of the fluid viscosity in the interfacial layer. The relaxation dynamics of polymer chains in shear flow was analyzed by evaluating the decay of time autocorrelation function of the first normal mode in the vorticity direction. We found that the rate behavior of the slip length correlates well with the inverse relaxation time of the polymer chains in the interfacial layer.

The rate-dependent slip boundary conditions were also reformulated in terms of the friction coefficient at the polymer/wall interface and slip velocity of the first fluid layer. In agreement with the results of the previous study [40], we found that the friction coefficient at lower melt densities undergoes a transition from a constant value to the power-law decay as a function of the slip velocity. At higher melt densities the friction coefficient decays as the power-law function in a wide range of slip velocities. When the magnitude of the surface-induced peak in the fluid structure factor is below a certain value, the friction coefficient is determined by a combination of parameters (structure factor, temperature, and contact density) of the first fluid layer near the solid wall.

ACKNOWLEDGMENTS

Financial support from the Petroleum Research Fund of the American Chemical Society is gratefully acknowledged. Computational work in support of this research was performed at Michigan State University's High Performance Computing Facility.

[1] C. M. Mate, *Tribology on the Small Scale: A Bottom Up Approach to Friction, Lubrication, and Wear* (Oxford University Press, New York, 2008).
[2] O. I. Vinogradova, Langmuir **11**, 2213 (1995).
[3] Y. Zhu and S. Granick, Phys. Rev. Lett. **88**, 106102 (2002).
[4] J. Sanchez-Reyes and L. A. Archer, Langmuir **19**, 3304 (2003).
[5] T. Schmatko, H. Hervet, and L. Leger, Langmuir **22**, 6843 (2006).
[6] O. I. Vinogradova and G. E. Yakubov, Phys. Rev. E **73**, 045302(R) (2006).
[7] N. V. Churaev, V. D. Sobolev, and A. N. Somov, J. Colloid Interface Sci. **97**, 574 (1984).
[8] J. Baudry, E. Charlaix, A. Tonck, and D. Mazuyer, Langmuir **17**, 5232 (2001).
[9] C. Cottin-Bizonne, S. Jurine, J. Baudry, J. Crassous, F. Restagno, and E. Charlaix, Eur. Phys. J. E **9**, 47 (2002).
[10] Y. Zhu and S. Granick, Phys. Rev. Lett. **87**, 096105 (2001).
[11] V. S. J. Craig, C. Neto, and D. R. M. Williams, Phys. Rev. Lett. **87**, 054504 (2001).
[12] Y. Zhu and S. Granick, Langmuir **18**, 10058 (2002).
[13] C. H. Choi, K. J. A. Westin, and K. S. Breuer, Phys. Fluids **15**, 2897 (2003).
[14] U. Ulmanella and C.-M. Ho, Phys. Fluids **20**, 101512 (2008).
[15] R. G. Horn, O. I. Vinogradova, M. E. Mackay, and N. Phan-Thien, J. Chem. Phys. **112**, 6424 (2000).
[16] T. Schmatko, H. Hervet, and L. Leger, Phys. Rev. Lett. **94**, 244501 (2005).
[17] F. Brochard and P. G. de Gennes, Langmuir **8**, 3033 (1992).
[18] K. B. Migler, H. Hervet, and L. Leger, Phys. Rev. Lett. **70**, 287 (1993).
[19] U. Heinbuch and J. Fischer, Phys. Rev. A **40**, 1144 (1989).
[20] J. Koplik, J. R. Banavar, and J. F. Willemsen, Phys. Fluids A **1**, 781 (1989).
[21] P. A. Thompson and M. O. Robbins, Phys. Rev. A **41**, 6830 (1990).
[22] J.-L. Barrat and L. Bocquet, Phys. Rev. Lett. **82**, 4671 (1999).
[23] J.-L. Barrat and L. Bocquet, Faraday Discuss. **112**, 119 (1999).
[24] M. Cieplak, J. Koplik, and J. R. Banavar, Phys. Rev. Lett. **86**, 803 (2001).
[25] V. P. Sokhan, D. Nicholson, and N. Quirke, J. Chem. Phys. **115**, 3878 (2001).
[26] T. M. Galea and P. Attard, Langmuir **20**, 3477 (2004).
[27] N. V. Priezjev, Phys. Rev. E **75**, 051605 (2007).
[28] N. V. Priezjev, J. Chem. Phys. **127**, 144708 (2007).
[29] P. A. Thompson and S. M. Troian, Nature (London) **389**, 360 (1997).
[30] S. C. Yang and L. B. Fang, Mol. Simul. **31**, 971 (2005).
[31] P. G. de Gennes, Rev. Mod. Phys. **57**, 827 (1985).
[32] N. V. Priezjev and S. M. Troian, Phys. Rev. Lett. **92**, 018302 (2004).
[33] E. Manias, G. Hadziioannou, I. Bitsanis, and G. ten Brinke, EPL **24**, 99 (1993).
[34] P. A. Thompson, M. O. Robbins, and G. S. Grest, Isr. J. Chem. **35**, 93 (1995).
[35] E. Manias, G. Hadziioannou, and G. ten Brinke, Langmuir **12**, 4587 (1996).
[36] R. Khare, J. J. de Pablo, and A. Yethiraj, Macromolecules **29**, 7910 (1996).
[37] M. J. Stevens, M. Mondello, G. S. Grest, S. T. Cui, H. D. Cochran, and P. T. Cummings, J. Chem. Phys. **106**, 7303 (1997).
[38] A. Koike and M. Yoneya, J. Phys. Chem. B **102**, 3669 (1998).
[39] A. Jabbarzadeh, J. D. Atkinson, and R. I. Tanner, J. Chem. Phys. **110**, 2612 (1999).
[40] A. Niavarani and N. V. Priezjev, Phys. Rev. E **77**, 041606 (2008).
[41] J. Servantie and M. Muller, Phys. Rev. Lett. **101**, 026101 (2008).
[42] M. Muller, C. Pastorino, and J. Servantie, J. Phys.: Condens. Matter **20**, 494225 (2008).
[43] A. Niavarani and N. V. Priezjev, J. Chem. Phys. **129**, 144902 (2008).
[44] R. B. Bird, C. F. Curtiss, R. C. Armstrong, and O. Hassager, *Dynamics of Polymeric Liquids*, 2nd ed. (Wiley, New York, 1987).
[45] K. Kremer and G. S. Grest, J. Chem. Phys. **92**, 5057 (1990).
[46] G. S. Grest and K. Kremer, Phys. Rev. A **33**, 3628 (1986).
[47] M. P. Allen and D. J. Tildesley, *Computer Simulation of Liquids* (Clarendon, Oxford, 1987).

[48] I. Bitsanis and G. Hadziioannou, J. Chem. Phys. **92**, 3827 (1990).
[49] J. H. Irving and J. G. Kirkwood, J. Chem. Phys. **18**, 817 (1950).
[50] A. Martini, H. Y. Hsu, N. A. Patankar, and S. Lichter, Phys. Rev. Lett. **100**, 206001 (2008).
[51] A. Martini, A. Roxin, R. Q. Snurr, Q. Wang, and S. Lichter, J. Fluid Mech. **600**, 257 (2008).
[52] N. V. Priezjev, A. A. Darhuber, and S. M. Troian, Phys. Rev. E **71**, 041608 (2005).
[53] N. V. Priezjev and S. M. Troian, J. Fluid Mech. **554**, 25 (2006).
[54] E. D. Smith, M. O. Robbins, and M. Cieplak, Phys. Rev. B **54**, 8252 (1996).
[55] M. S. Tomassone, J. B. Sokoloff, A. Widom, and J. Krim, Phys. Rev. Lett. **79**, 4798 (1997).
[56] D. Mukherji and M. H. Muser, Phys. Rev. E **74**, 010601(R) (2006).
[57] T. Aoyagi, J. Takimoto, and M. Doi, J. Chem. Phys. **115**, 552 (2001).
[58] I. A. Bitsanis and C. Pan, J. Chem. Phys. **99**, 5520 (1993).
[59] K. Binder, *Monte Carlo and Molecular Dynamics Simulations in Polymer Science* (Oxford University Press, New York, 1995).